

Spectroscopic study of red giants in the *Kepler* field with asteroseismologically established evolutionary status and stellar parameters

Y. Takeda^{1*}† and A. Tajitsu²

¹*National Astronomical Observatory of Japan, 2-21-1 Osawa, Mitaka, Tokyo 181-8588, Japan*

²*Subaru Telescope, 650 N. A'ohoku Place, Hilo, HI 96720, U.S.A.*

Accepted 2015 March 25. Received 2015 March 5; in original form 2015 February 3

ABSTRACT

Thanks to the recent very high-precision photometry of red giants from satellites such as *Kepler*, precise mass and radius values as well as accurate information of evolutionary stages are already established by asteroseismic approach for a large number of G–K giants. Based on the high-dispersion spectra of selected such 55 red giants in the *Kepler* field with precisely known seismic parameters (among which parallaxes are available for 9 stars), we checked the accuracy of the determination method of stellar parameters previously applied to many red giants by Takeda et al. (2008, PASJ, 60, 781), since it may be possible to discriminate their complex evolutionary status by using the surface gravity vs. mass diagram. We confirmed that our spectroscopic gravity and the seismic gravity satisfactorily agree with each other (to within $\simeq 0.1$ dex) without any systematic difference. However, the mass values of He-burning red clump giants derived from stellar evolutionary tracks ($\sim 2\text{--}3\text{ M}_{\odot}$) were found to be markedly larger by $\sim 50\%$ compared to the seismic values ($\sim 1\text{--}2\text{ M}_{\odot}$) though such discrepancy is not seen for normal giants in the H-burning phase, which reflects the difficulty of mass determination from intricately overlapping tracks on the luminosity vs. effective temperature diagram. This consequence implies that the mass results of many red giants in the clump region determined by Takeda et al. (2008) are likely to be significantly overestimated. We also compare our spectroscopically established parameters with recent literature values, and further discuss the prospect of distinguishing the evolutionary status of red giants based on the conventional (i.e., non-seismic) approach.

Key words: stars: abundances – stars: atmospheres – stars: evolution – stars: late-type – stars: oscillations

1 INTRODUCTION

Red giant stars are low-to-intermediate mass ($\sim 1\text{--}5\text{ M}_{\odot}$) stars which have already evolved off the main sequence with lowered temperature as well as inflated radius, currently situating in the high luminosity ($L \sim 10\text{--}1000\text{ L}_{\odot}$) and late spectral type ($T_{\text{eff}} \sim 4000\text{--}5500\text{ K}$) region in the HR diagram. Since they are intrinsically bright and numerous in number while covering a wide range of age, their astrophysical importance is widely known (e.g., as probes of galactic chemical evolution).

One notorious problem regarding red giants is that an inevitable ambiguity is involved in understanding their evolutionary status. As shown in Fig. 1, normal giants of the red giant branch (RGB) in the shell H-burning phase (C \rightarrow D) and the He-core burning giants of the asymptotic giant branch (AGB: E \rightarrow F and further) follow almost same track in the HR diagram, which makes understanding the evolutionary status of a given star very difficult based on the position on this diagram alone. Especially important are the red-clump (RC) giants (around E), which have just started stable core He burning after the He-ignition (D \rightarrow E) and are bound to gradually ascend the AGB. They tend to cluster at a fixed luminosity because of their comparatively slow evolution, and thus making up a considerably large fraction of red giants. But it is very hard to tell only from the HR

* E-mail: takeda.yoichi@nao.ac.jp

† Based on data collected at Subaru Telescope, which is operated by the National Astronomical Observatory of Japan.

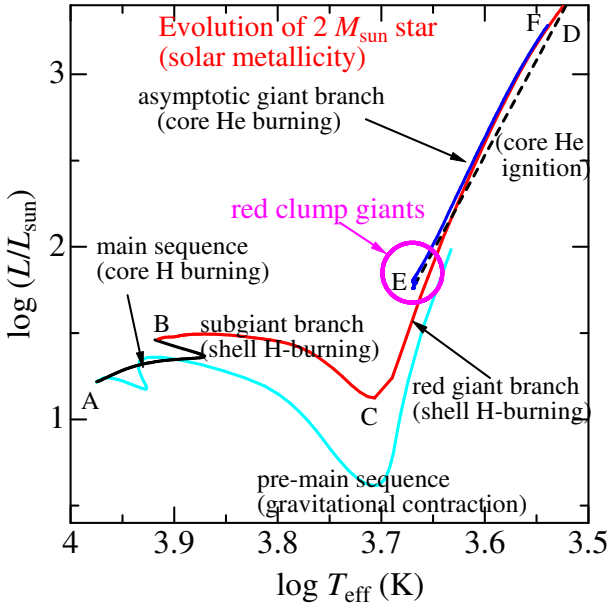


Figure 1. Typical evolutionary track of red giants on the $\log L$ vs. $\log T_{\text{eff}}$ diagram. Shown here is the case of a $2 M_{\odot}$ star of solar metallicity calculated by Lagarde et al. (2012).

diagram whether a given star in this red clump region is a real RC star or a normal RGB star just wandering into this area.

Fortunately, recent progress in asteroseismology has shed light on this stagnant situation. The extremely high-precision photometry accomplished by satellite observations (such as *CoRoT* or *Kepler*) has made it possible to detect very subtle photometric variability of red giants pulsating in the mixed p- and g-mode. It then revealed that normal giants and red-clump giants were clearly distinguished (by using the $\Delta\nu$ vs. $\Delta\Pi_1$ diagram) and mass as well as radius could be precisely determined (from ν_{max} and $\Delta\nu$ with the help of the scaling relations) by analyzing the power spectrum of their oscillation. In this way, Mosser et al. (2012) successfully classified many G–K giants in the *Kepler* field into three categories of (a) normal red giants (RG: before He ignition), (b) 1st clump giants (RC1: ordinary RC stars of comparatively lower mass after degenerate He-ignition), and (c) 2nd clump giants (RC2: RC stars of comparatively higher mass after non-degenerate He-ignition; cf. Girardi 1999), and published their asteroseismic radius (R_{seis}) and mass (M_{seis}) values.

Yet, while such an achievement of distinguishing RG/RC1/RC2 by way of asteroseismology is surely a great benefit for the astronomical community, such a special technique of very high-precision photometry is not always applicable. Is it possible to find a way based on the conventional method to discriminate the evolutionary status of red giants in general?

Takeda, Sato & Murata (2008, hereinafter referred to as Paper I) conducted an extensive stellar parameter study for apparently bright ($V < 6.5$) 322 field giants, for which atmospheric parameters [the effective temperature (T_{eff}), surface gravity ($\log g$), microturbulence (v_t), and metallicity ($[\text{Fe}/\text{H}]$)] were spectroscopically determined from Fe I and Fe II lines. The stellar age (*age*) and mass (*M*) were derived

by comparing their positions on the HR diagram ($\log L$ vs. $\log T_{\text{eff}}$) with theoretical evolutionary tracks, where the luminosity (*L*) was evaluated with the help of Hipparcos parallaxes (ESA 1997).

As a probe, we compared the relations between the parameters ($\log L$ vs. $\log T_{\text{eff}}$, $\log g$ vs. *M*, and $\log g$ vs. *R*) of 322 red giants studied in Paper I and those corresponding to Mosser et al.’s (2012) 218 samples in the *Kepler* field (with well established parameters and evolutionary status), as depicted in Fig. 2. Then, an interesting similarity (i.e., the characteristic “trifid” structure) is noticed between Fig. 2b and Fig. 2e, which suggests a possibility that $\log g$ and *M* values determined in such an ordinary manner as in Paper I may be used to clarify (or at least guess) the evolutionary status of a red giant from its position on the $\log g$ vs. *M* diagram. If this is confirmed to be practically feasible, it would be very useful.

However, some concerns still exist. First, we do not yet have much confidence as to whether the spectroscopic $\log g$ values determined in Paper I are sufficiently reliable, since they tend to be systematically lower by ~ 0.2 – 0.3 dex as compared to various literature values despite of being derived in a similar way (cf. Sect. 3.3 in Paper I; especially Figs. 5b, 6b, 7b, and 8b therein). Second, the intersection of the “trifid” structure is located at ~ 1.5 – $2 M_{\odot}$ for Mosser et al.’s (2012) sample (Fig. 2b), while at an appreciably larger mass around $\sim 2.5 M_{\odot}$ for those in Paper I (Fig. 2e). This difference makes us wonder whether the mass values derived from evolutionary tracks are really correct.

Thus, as a first preparatory step toward our intended goal, we decided to carry out a spectroscopic study for a number of red giant stars in the *Kepler* field (with well-established evolutionary stage and $M_{\text{seis}}/R_{\text{seis}}/\log g_{\text{seis}}$) selected from Mosser et al.’s (2012) sample. Based on the high-dispersion spectra primarily obtained with Subaru/HDS, their parameters were determined (while following the same manner as in Paper I) and compared with the seismic values, by which we may be able to check the accuracy level of our parameter determination procedures. This was the original motivation of the present study, and the purpose of this article is report the outcome of the investigation.

2 OBSERVATIONAL DATA

The targets in this investigation were exclusively taken from Mosser et al.’s (2012) 218 red giants in the *Kepler* field, for which the evolutionary status is well established in asteroseismic manner along with R_{seis} and M_{seis} . The observations of 42 stars (with their *Kepler* magnitudes being ~ 9 – 11 mag) selected from this list were carried out on 2014 September 9 (UT) with the High Dispersion Spectrograph (HDS; Noguchi et al. 2002) placed at the Nasmyth platform of the 8.2-m Subaru Telescope, by which high-dispersion spectra covering ~ 5100 – 7800 Å were obtained (with two CCDs of $2K \times 4K$ pixels) in the standard StdRa setting with the red cross disperser. We used the Image Slicer #2 (Tajitsu, Aoki & Yamamuro 2012), which resulted in a spectrum resolving power of $R \simeq 80000$. The total exposure time per star was from a few minutes to ~ 10 min in most cases.

The reduction of the spectra (bias subtraction, flat-fielding, scattered-light subtraction, spectrum extraction,

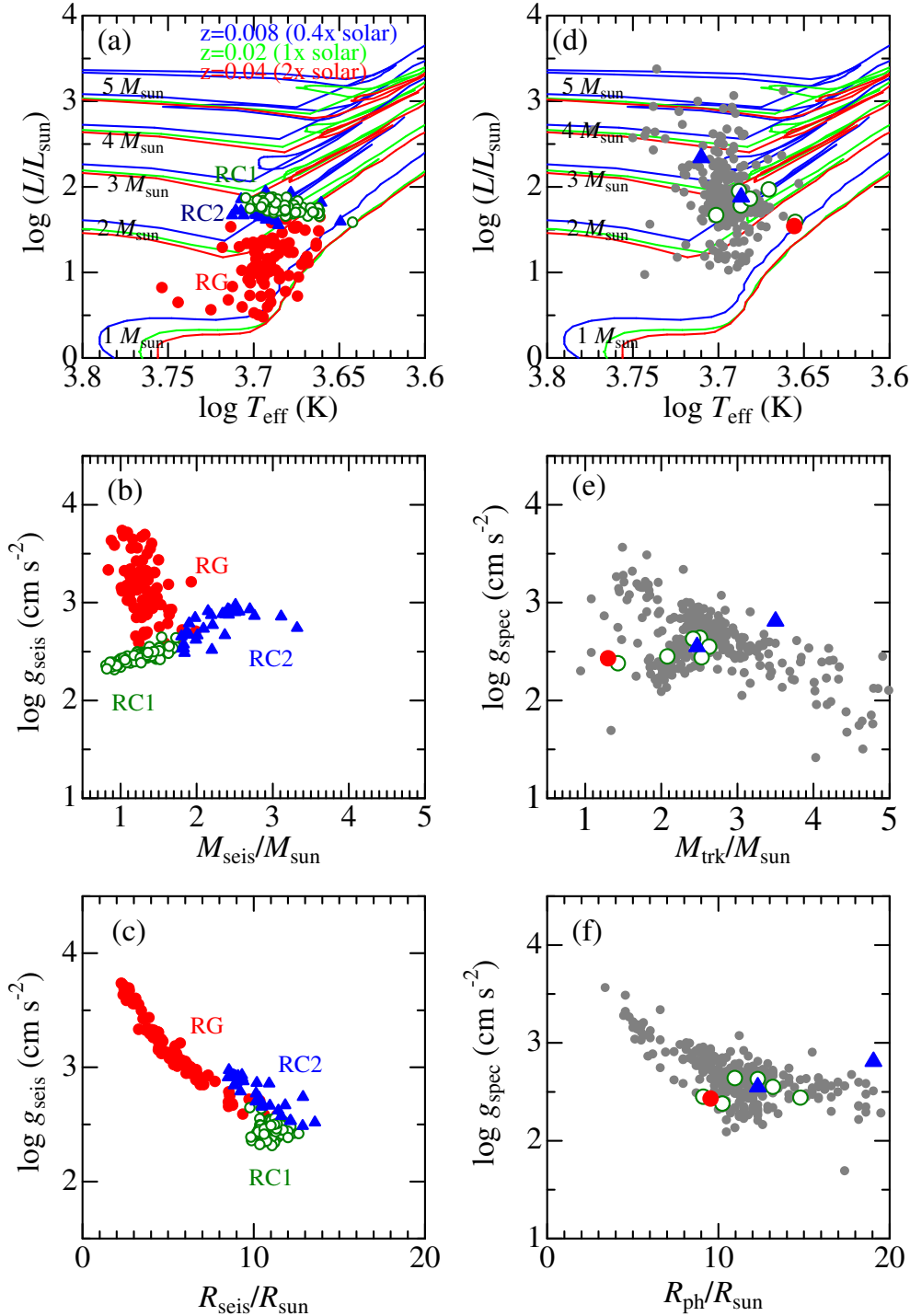


Figure 2. Upper (a, d), middle (b, e), and lower (c, f) panels show the diagrams of $\log L$ vs. $\log T_{\text{eff}}$ (with theoretical evolutionary tracks computed by Lejeune & Schaerer 2001), $\log g$ vs. M , and $\log g$ vs. R , respectively. The left panels (a, b, c) are constructed from the seismic results of 218 giants published by Mosser et al. (2012), where different symbols correspond to each evolutionary class: filled circles ... normal red giants (RG), open circles ... 1st clump giants (RC1), and filled triangles ... 2nd clump giants. In panel (a), Brown et al.'s (2011) T_{eff} (KIC) values were used for the abscissa as well as for evaluation of L . In the right panels (d, e, f) are plotted the results of 322 giants studied in Paper I [panels (d) and (e) here are same as Fig. 2 and Fig. 3e therein], where T_{eff} and $\log g$ were spectroscopically determined, L and R are the photometric values (cf. caption of Table 2), and M was estimated in comparison with evolutionary tracks. In addition, the results of 9 stars (among our 55 program stars) with known parallaxes (see Table 2) are also overplotted in panels (d), (e), and (f), which will be discussed in Sect. 4.2.

wavelength calibration, co-adding of frames to improve S/N, continuum normalization) was performed by using the “echelle” package of the software IRAF¹ in a standard manner. Typical S/N ratios attained in the final spectra are ~ 100 –200.

In addition to these Subaru/HDS data, we also used the spectra of *Kepler* red giants published by Thygesen et al. (2012), which they obtained with Nordic Optical Telescope (NOT; $R \simeq 67000$, 3700 – 7300 Å, $S/N \simeq 80$ –100), Canada-France-Hawaii Telescope (CFHT; $R \simeq 80000$, 3700 – 10500 Å, $S/N \simeq 200$), and Telescope Bernard Lyot (TBL; $R \simeq 75000$, 3700 – 10500 Å, $S/N \simeq 200$). Since 16 stars (out of their 82 stars) are included in Mosser et al.’s (2012) list (218 stars), we used their spectra for these 16 stars. Note that the spectra for three stars (KIC 1726211, KIC 2714397, and KIC 3744043) are commonly available in both samples of ours as well as Thygesen et al.’s, which means that the net number of our targets is 55 ($= 42 + 16 - 3$). The spectra for these three stars in the orange region (around ~ 6085 Å) are displayed in Fig. 3 for comparison. The complete target list and the distinction of data source [ours \cdots “Subaru”, Thygesen et al. \cdots “NOT” or “CFHT/TBL”]² is given in Table 1.

3 PARAMETER DETERMINATIONS

3.1 Atmospheric parameters

The determination of the atmospheric parameters (T_{eff} , $\log g$, v_t and $[\text{Fe}/\text{H}]$) was implemented in the same manner as in Paper I (see Sect. 3.1 for the details) by applying the program TGVIT (Takeda et al. 2005; cf. Sect. 2 therein), which is based on the principles described in Takeda, Ohkubo & Sadakane (2002), to the equivalent widths (W_λ) of Fe I and Fe II lines measured on the spectrum of each star by the Gaussian-fitting method. As before, we restricted to using lines satisfying $W_\lambda \leq 120$ mÅ and those showing abundance deviations from the mean larger than 2.5σ were rejected. The final number of adopted lines are ~ 200 (Fe I) and ~ 15 (Fe II) on the average. The resulting final solutions are presented in Table 1, while $\log \epsilon(\text{Fe})$ values (Fe abundances corresponding to the final solutions) are plotted against W_λ and χ_{low} in Fig. 4 and Fig. 5, respectively, where we can see that the required conditions [i.e., no systematic dependence of $\log \epsilon(\text{Fe})$ upon W_λ as well as χ_{low} , and the equality of $\langle \log \epsilon(\text{Fe I}) \rangle = \langle \log \epsilon(\text{Fe II}) \rangle$ (ionization equilibrium)] are reasonably accomplished. The internal statistical errors involved with these solutions are almost the same order as the case of Paper I. The detailed W_λ and $\log \epsilon(\text{Fe})$ data for each star are given in tableE1.dat (supplementary online material).

¹ IRAF is distributed by the National Optical Astronomy Observatories, which is operated by the Association of Universities for Research in Astronomy, Inc. under cooperative agreement with the National Science Foundation.

² We could not distinguish whether Thygesen et al.’s (2012) spectra covering wide wavelength region (3700 – 10500 Å) correspond to which of CFHT or TBL, since the details are not specified. Therefore, we simply noted as “CFHT/TBL” for the relevant cases.

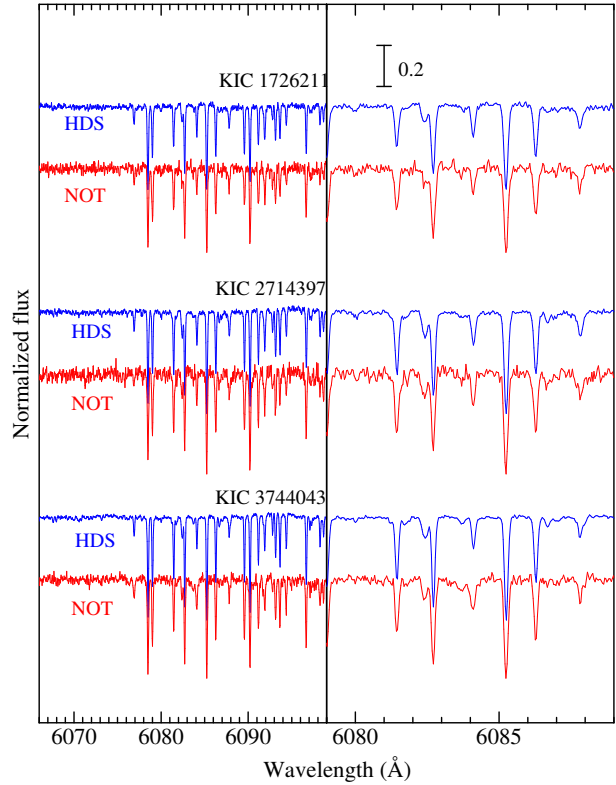


Figure 3. Comparison of the representative spectra used in this study. Shown are the spectral portions in the 6066–6099 Å region (left panel) and the 6079–6089 Å region (right panel) for KIC 1726211, KIC 2714397, and KIC 3744043, for which Subaru/HDS spectra (based on our observation) and NOT spectra (published by Thygesen et al. 2012) are doubly available. Each spectrum is appropriately shifted relative to the adjacent one. The wavelength scale is adjusted to the laboratory frame.

3.2 Rotational velocity

Given such established atmospheric parameters, we constructed the model atmospheres for each of the program stars as done in Paper I. Then, based on these atmospheric models, the projected rotational velocity ($v_e \sin i$) of each star was determined from the width of the macrobroadening function (consisting of combined effects of instrumental broadening, macroturbulence broadening, and rotational broadening), which was derived from the spectrum-fitting in the 6080–6089 Å region in the same way as done in Paper I (cf. Sect. 4.2 therein for more details). Fig. 6 shows how the best-fit theoretical spectrum matches the observed spectrum for each star. The resulting $v_e \sin i$ values are presented in Table 1. Besides, the detailed values of the relevant broadening widths (the instrumental width and the macroturbulence width estimated from $\log g$, which are to be subtracted from the total broadening) are given in tableE2.dat (supplementary online material), where the elemental abundances of Si, Ti, V, Fe, Co, and Ni obtained as by-products are also given.³

³ Since chemical abundances are outside of the scope of this paper, we refrain from discussing these results further on. We only note that the resulting $[\text{X}/\text{Fe}]$ vs. $[\text{Fe}/\text{H}]$ relations for these el-

Table 1. Basic data and the resulting parameters of the program stars.

KIC# (1)	Kepler (2)	T_{eff} (3)	$\log g$ (4)	v_t (5)	[Fe/H] (6)	ν_{max} (7)	$\Delta\nu$ (8)	$\Delta\Pi_1$ (9)	R_{seis} (10)	M_{seis} (11)	$\log g_{\text{seis}}$ (12)	$v_e \sin i$ (13)	class (14)	Source (15)
[Results based on our Subaru/HDS spectra]														
01726211	10.93	4983	2.49	1.34	-0.57	29.0	3.72	326.10	11.62	1.19	2.39	2.5	RC1	Subaru
02013502	11.91	4913	2.69	1.14	-0.02	61.0	5.72	232.20	10.26	1.94	2.71	2.8	RC2	Subaru
02303367	10.18	4601	2.39	1.36	+0.06	34.2	4.05	308.70	11.11	1.23	2.44	2.2	RC1	Subaru
02424934	10.38	4792	2.48	1.31	-0.18	33.0	3.91	328.50	11.73	1.36	2.43	2.1	RC1	Subaru
02448225	10.81	4577	2.37	1.32	+0.16	38.2	3.96	285.50	12.94	1.87	2.49	2.4	RC2	Subaru
02714397	10.51	4910	2.56	1.38	-0.47	33.0	4.14	326.70	10.59	1.12	2.44	2.4	RC1	Subaru
03217051	11.38	4590	2.44	1.27	+0.21	36.0	4.22	314.50	10.75	1.22	2.46	2.4	RC1	Subaru
03455760	10.94	4654	2.68	1.13	-0.07	48.0	4.89	64.30	10.75	1.63	2.59	2.1	RG	Subaru
03730953	8.82	4861	2.55	0.97	-0.07	50.3	4.91	308.60	11.42	1.97	2.62	2.8	RC2	Subaru
03744043	9.66	4946	2.94	1.10	-0.35	110.9	9.90	75.98	6.25	1.31	2.97	1.6	RG	Subaru
03758458	11.28	5009	2.71	1.28	+0.07	65.0	5.87	262.62	10.48	2.18	2.74	2.6	RC2	Subaru
04036007	11.43	4916	2.42	1.33	-0.36	38.0	4.37	307.99	10.96	1.38	2.50	2.2	RC1	Subaru
04044238	7.83	4519	2.38	1.32	+0.20	33.0	4.07	296.35	10.52	1.06	2.42	2.2	RC1	Subaru
04243623	11.17	5005	3.75	0.74	-0.31	495.6	32.80	118.20	2.56	0.99	3.62	1.9	RG	Subaru
04243796	10.80	4620	2.34	1.34	+0.11	37.0	4.28	296.27	10.78	1.26	2.48	2.1	RC1	Subaru
04351319	9.94	4876	3.32	0.91	+0.29	386.0	24.50	98.70	3.53	1.45	3.51	2.1	RG	Subaru
04445711	10.72	4876	2.50	1.38	-0.32	37.0	4.29	333.30	11.02	1.35	2.49	2.3	RC1	Subaru
04770846	9.54	4847	2.60	1.27	+0.02	53.9	5.46	308.12	9.88	1.58	2.65	2.5	RC1	Subaru
04902641	10.76	4987	2.84	1.15	+0.03	101.6	7.87	147.28	9.10	2.56	2.93	2.2	RC2	Subaru
04952717	11.23	4793	3.13	0.93	+0.13	202.1	15.58	87.52	4.53	1.24	3.22	1.6	RG	Subaru
05000307	11.23	5023	2.64	1.27	-0.25	42.2	4.74	323.70	10.45	1.41	2.55	2.9	RC1	Subaru
05033245	10.91	5049	3.41	0.97	+0.11	424.2	26.82	114.20	3.29	1.41	3.55	2.1	RG	Subaru
05088362	11.15	4760	2.41	1.33	+0.03	40.1	3.99	230.95	13.65	2.22	2.52	2.1	RC2	Subaru
05128171	10.10	4808	2.54	1.30	+0.04	56.1	5.27	319.59	11.00	2.03	2.66	2.4	RC2	Subaru
05266416	10.61	4767	2.50	1.33	-0.09	32.4	3.75	284.37	12.49	1.51	2.42	2.3	RC1	Subaru
05307747	8.40	5031	2.77	1.27	+0.01	88.2	6.88	296.30	10.38	2.91	2.87	2.6	RC2	Subaru
05530598	8.72	4599	2.85	1.04	+0.37	105.5	8.72	76.30	7.39	1.68	2.93	2.1	RG	Subaru
05723165	10.60	5255	3.67	0.90	-0.02	578.8	34.67	127.30	2.74	1.36	3.70	2.2	RG	Subaru
05737655	7.20	5026	2.45	1.46	-0.63	29.8	4.24	278.60	9.23	0.78	2.40	4.0	RC1	Subaru
05806522	11.26	4574	2.60	1.09	+0.12	56.0	5.92	69.47	8.49	1.18	2.65	1.8	RG	Subaru
05866737	10.76	4874	2.86	1.14	-0.26	67.6	6.55	59.51	8.64	1.52	2.75	1.8	RG	Subaru
05990753	10.92	5011	2.97	1.15	+0.19	97.9	7.57	195.00	9.50	2.70	2.92	3.4	RC2	Subaru
06117517	10.59	4649	2.94	0.97	+0.28	116.9	10.16	76.91	6.06	1.26	2.98	1.8	RG	Subaru
06144777	10.69	4734	3.02	1.02	+0.14	126.0	11.01	69.91	5.62	1.18	3.01	1.9	RG	Subaru
06276948	10.83	4939	2.84	1.18	+0.19	91.6	7.41	259.00	9.21	2.35	2.88	2.6	RC2	Subaru
07205067	10.72	5064	2.58	1.32	+0.03	66.0	5.30	278.60	13.13	3.49	2.75	3.8	RC2	Subaru
07581399	11.49	5070	2.74	1.14	+0.01	85.0	6.59	222.00	10.94	3.13	2.86	3.3	RC2	Subaru
08378462	11.13	4995	2.81	1.19	+0.06	90.3	7.27	238.30	9.48	2.47	2.88	2.1	RC2	Subaru
08702606	9.29	5472	3.66	1.01	-0.11	630.3	39.70	177.00	2.32	1.09	3.74	2.7	RG	Subaru
08718745	10.71	4902	3.20	0.98	-0.25	129.4	11.40	79.45	5.47	1.17	3.03	1.8	RG	Subaru
09173371	9.27	5064	2.85	1.18	+0.00	98.9	7.95	236.34	8.74	2.32	2.92	2.9	RC2	Subaru
11819760	10.80	4824	2.36	1.32	-0.18	29.1	3.64	296.20	11.98	1.25	2.38	1.8	RC1	Subaru
[Results based on Thygesen et al.'s (2012) spectra]														
01726211	10.93	4933	2.37	1.33	-0.57	29.0	3.72	326.10	11.56	1.17	2.38	2.3	RC1	NOT
02714397	10.51	4956	2.77	1.39	-0.36	33.0	4.14	326.70	10.64	1.14	2.44	2.0	RC1	NOT
03744043	9.66	4938	2.88	1.05	-0.28	110.9	9.90	75.98	6.24	1.31	2.97	1.6	RG	NOT
03748691	11.59	4762	2.53	1.31	+0.11	37.0	4.24	299.60	11.15	1.37	2.48	2.2	RC1	NOT
05795626	9.16	4923	2.38	1.30	-0.72	37.2	4.45	311.10	10.35	1.21	2.49	2.5	RC1	NOT
06690139	11.67	4979	3.02	1.06	-0.14	113.8	9.69	66.90	6.72	1.56	2.98	1.9	RG	NOT
08813946	7.03	4862	2.64	1.27	+0.09	72.8	6.39	255.40	9.76	2.09	2.78	3.0	RC1	CFHT/TBL
09705687	9.58	5129	2.81	1.26	-0.19	72.3	6.62	255.90	9.28	1.92	2.79	2.5	RC2	NOT
10323222	6.72	4525	2.43	1.18	+0.04	47.7	4.88	61.25	10.58	1.55	2.58	2.0	RG	CFHT/TBL
10404994	7.42	4803	2.63	1.26	-0.06	40.3	4.43	297.00	11.17	1.50	2.52	2.6	RC1	CFHT/TBL
10426854	9.94	4968	2.52	1.34	-0.30	40.9	4.35	318.00	11.96	1.78	2.53	2.6	RC1	NOT
10716853	6.89	4874	2.55	1.27	-0.08	48.8	4.95	296.00	10.92	1.75	2.61	2.2	RC1	CFHT/TBL
11444313	11.31	4757	2.52	1.36	+0.00	34.2	3.98	315.20	11.69	1.39	2.45	2.4	RC1	NOT
11569659	11.51	4879	2.48	1.36	-0.26	29.2	4.04	292.60	9.81	0.85	2.38	2.6	RC1	NOT
11657684	11.71	4951	2.47	1.29	-0.12	33.7	4.09	291.30	11.13	1.27	2.45	1.9	RC1	NOT
12884274	7.59	4683	2.44	1.35	+0.11	41.4	4.57	323.20	10.65	1.39	2.53	2.4	RC1	CFHT/TBL

Following the serial number and the *Kepler* magnitude (in mag) of the *Kepler* Input Catalogue (KIC; cf. Brown et al. 2011) in Columns (1) and (2), the atmospheric parameters (effective temperature T_{eff} in K, logarithmic surface gravity $\log g$ in $\text{cm s}^{-2}/\text{dex}$, microturbulent velocity dispersion v_t in km s^{-1} , and metallicity [Fe/H] in dex) spectroscopically determined from Fe I and Fe II lines are presented in Columns (3)–(6). Columns (7)–(9) give the asteroseismic quantities (expressed in μHz) taken from Mosser et al. (2012): the central frequency of the oscillation power excess (ν_{max}), the large frequency separation ($\Delta\nu$), and the gravity-mode spacing ($\Delta\Pi_1$; good indicator for discriminating between RG and RC1/RC2). Presented in Columns (10)–(12) are the seismic radius (in R_{\odot}), seismic mass (in M_{\odot}), and the corresponding seismic surface gravity (in $\text{cm s}^{-2}/\text{dex}$, which were evaluated from ν_{max} and $\Delta\nu$ by using the scaling relations [Eqs. (1)–(3)]. In Columns (13) and (14) are given the projected rotational velocity (in km s^{-1} ; derived from the 6080–6089 Å fitting analysis) and the evolutionary class determined by Mosser et al. (2012) (RG: red giant, RC1: 1st clump giant, RC2: 2nd clump giant). Column (15) gives the data source (cf. Sect. 2 and footnote 2) of the spectrum.

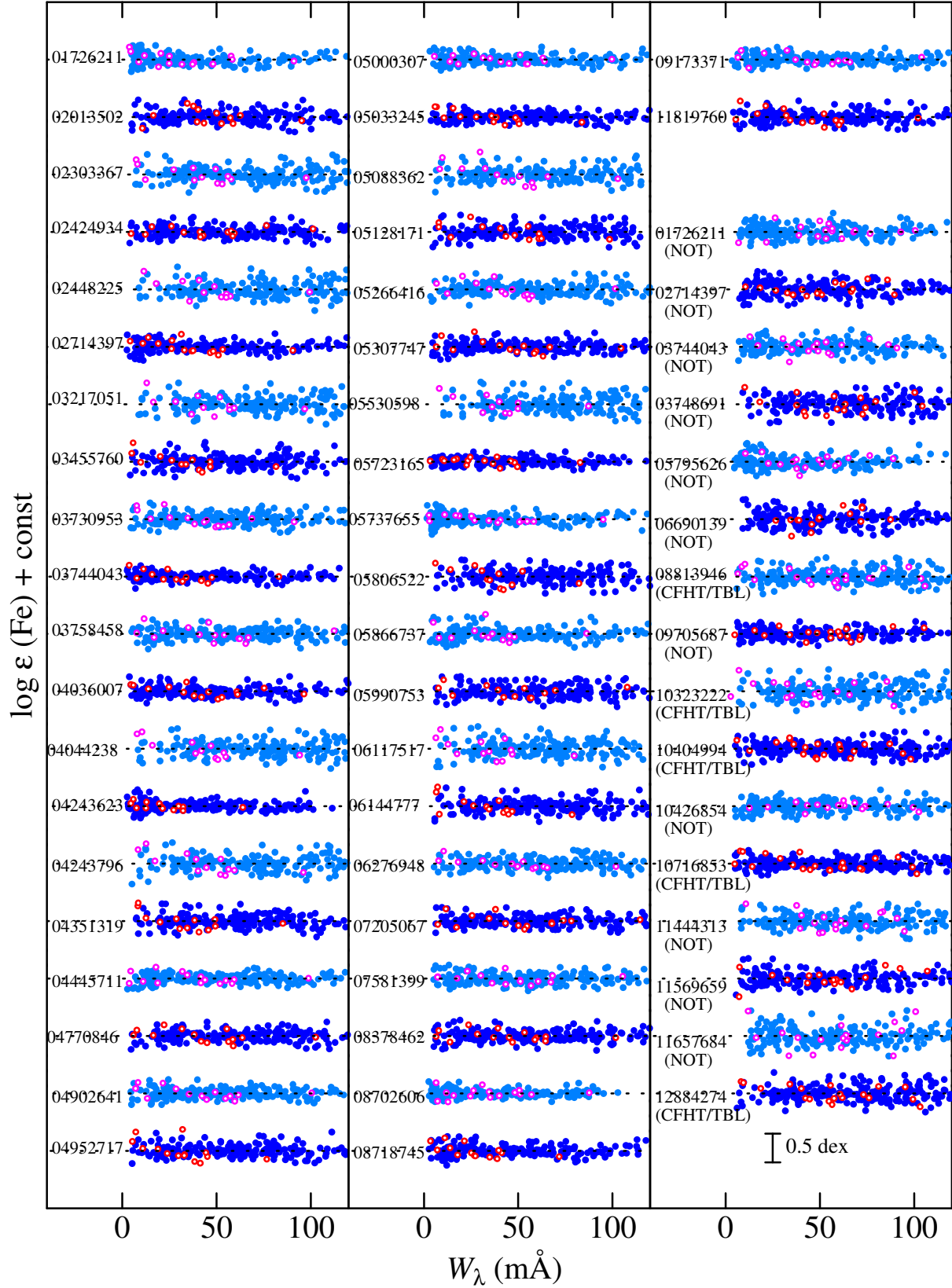


Figure 4. Fe abundance vs. equivalent width relations corresponding to the finally established atmospheric parameters of T_{eff} , $\log g$, and v_t for each of the 58 stars, being arranged in the same order as in Table 1 as indicated by the KIC number. The filled and open symbols correspond to Fe I and Fe II lines, respectively. The results for each star are shown relative to the mean abundance indicated by the horizontal dotted line, and vertically shifted by 1.0 relative to the adjacent ones.

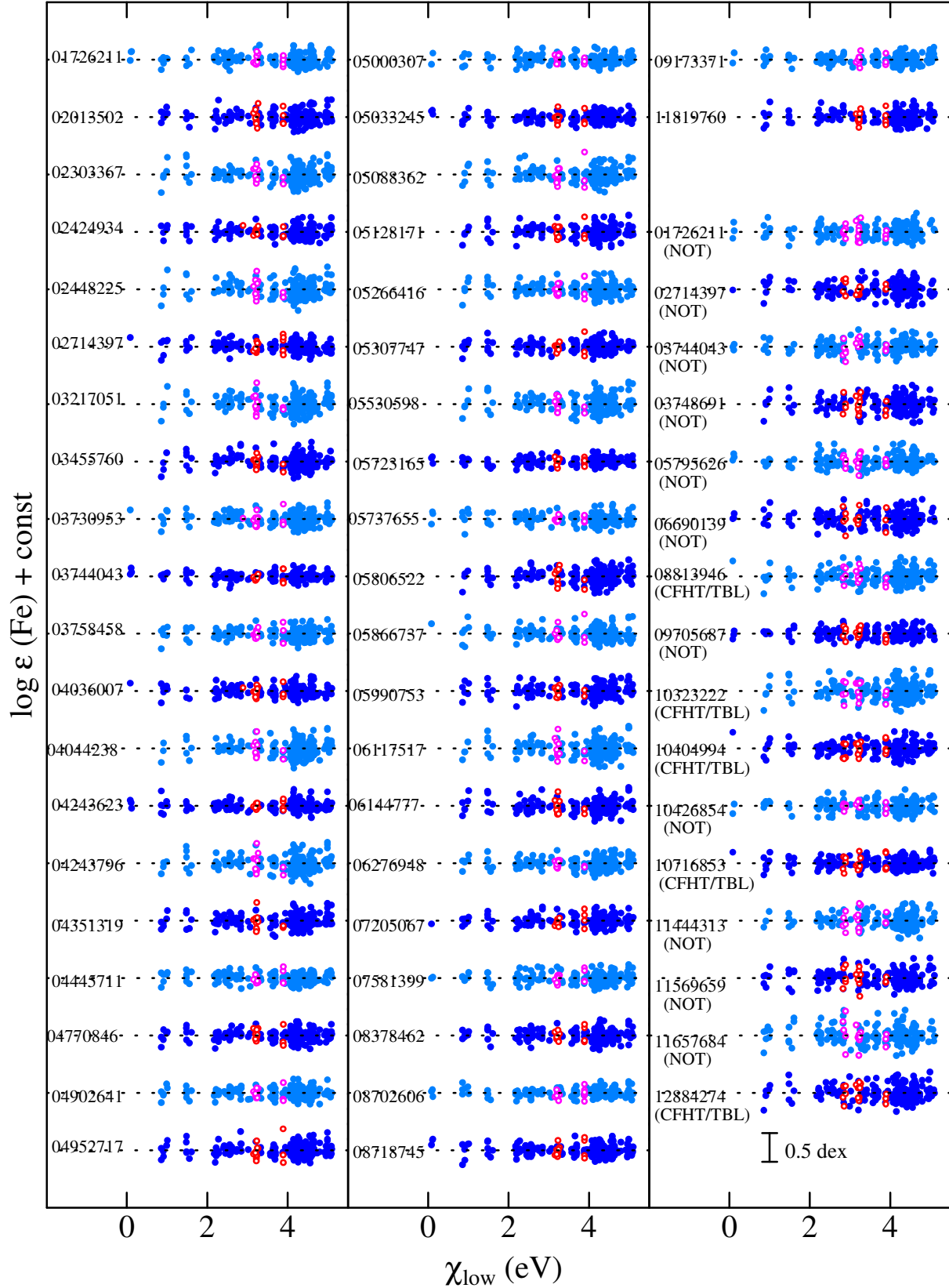


Figure 5. Fe abundance vs. lower excitation potential relations corresponding to the finally established atmospheric parameters for each of the 58 stars. Otherwise, the same as in Fig. 4.

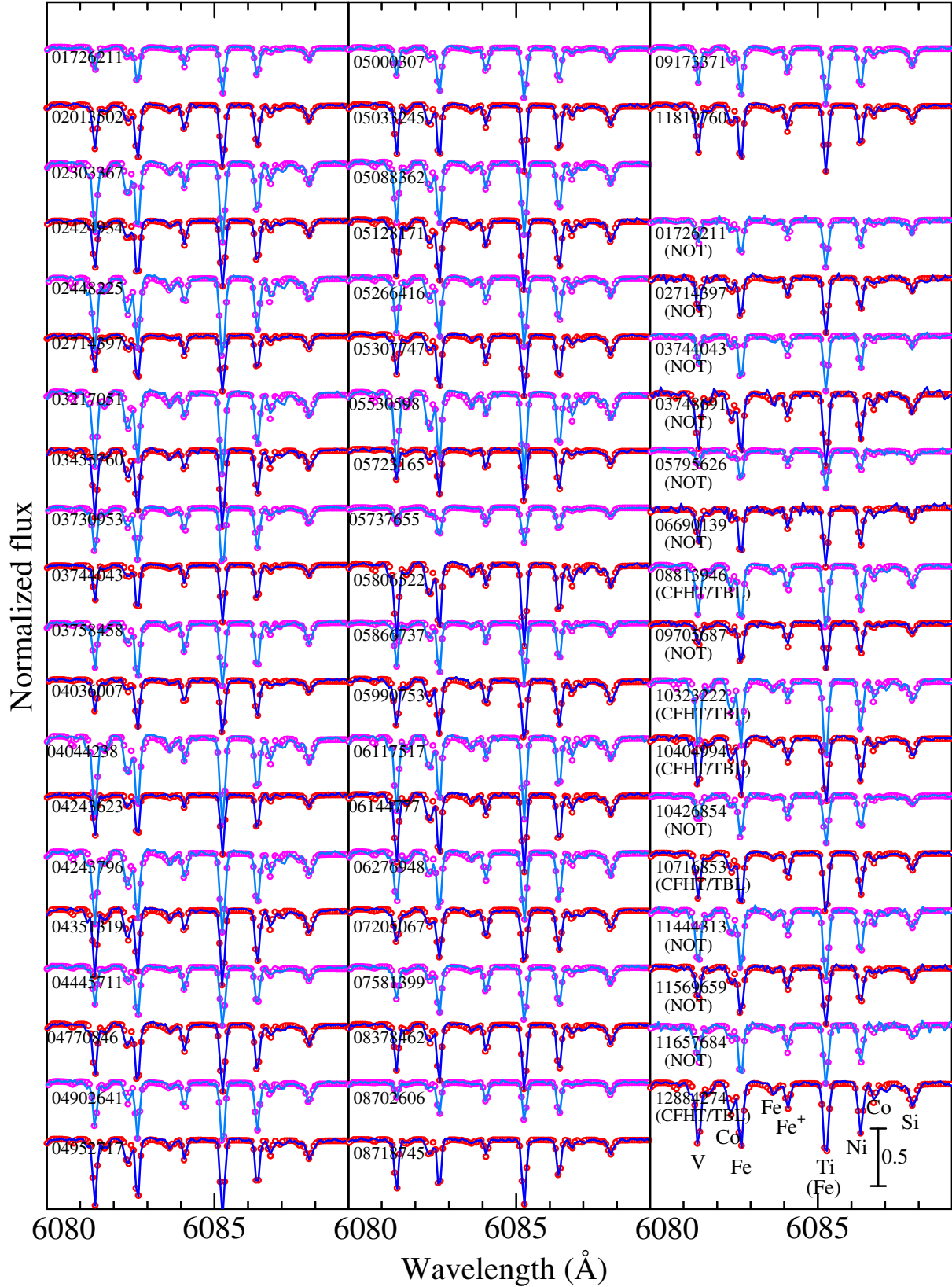


Figure 6. Synthetic spectrum fitting in the 6080–6089 Å region accomplished by varying the abundances of Si, Ti, V, Fe, Co, and Ni, along with the macrobroadening velocity (v_M) and the wavelength shift (radial velocity). The best-fit theoretical spectra are shown by solid lines, while the observed data are plotted by symbols, where the wavelength scale of the stellar spectrum has been adjusted to the laboratory frame. In each panel, the spectra are arranged in the same order as in Table 1 (corresponding KIC numbers are indicated), and each spectrum is vertically shifted by 0.5 relative to the adjacent one.

3.3 Parameters related to HR diagram

Unfortunately, distances are not necessarily known for all our 55 targets, in which Hipparcos parallax data (ESA 1997) are available for only 9 comparatively bright stars (KIC 03730953, 04044238, 05737655, 08813946, 09705687, 10323222, 10404994, 10716853, 12884274). We derived various stellar parameters (luminosity, radius, and mass) relevant to the HR diagram for these stars with the help of Lejeune & Schaerer’s (2001) theoretical evolutionary tracks in the same manner as done in Paper I (cf. Sect. 3.2 therein), which are summarized in Table 2. Such derived quantities for these 9 stars are also overplotted in Figs. 2d–2f. Note that the results for KIC 09705687 (HIP 94976) are considered to be less reliable, since its parallax contains a large error (larger than the parallax value itself).

3.4 Comparison with previous studies

Fig. 7 shows the comparison of our spectroscopic T_{eff} , $\log g$, and $[\text{Fe}/\text{H}]$ with those given in the *Kepler* Input Catalogue (Brown et al. 2011) which were estimated in the photometric way using color indices. We can state that almost the same conclusion as reported by Thygesen et al. (2012) can be drawn from this comparison; i.e., a rough consistency can be seen (i.e., the correlation coefficient is $r \sim 0.7$; cf. Table 3) but very large discrepancies are sometimes observed, and the differences tend to be weakly T_{eff} -dependent.⁴

It is worth comparing our established parameters with those determined by Thygesen et al. (2012), since they are based on the same observational material as well as similar spectroscopic techniques. Such comparisons of T_{eff} , $\log g$, v_t , $[\text{Fe}/\text{H}]$, and $v_e \sin i$ for 16 stars are displayed in Fig. 8. We can see that both are in more or less reasonable agreement for T_{eff} , $\log g$, v_t , and $[\text{Fe}/\text{H}]$ ($r \sim 0.7$ – 0.9 ; cf. Table 3), though our v_t tends to be systematically smaller by ~ 0.1 – 0.2 km s^{-1} and our T_{eff} is slightly lower by $\sim 100 \text{ K}$. However, our $v_e \sin i$ values are in distinct disagreement with no meaningful correlation ($r = 0.25$) with those derived by Thygesen et al. (2012), in the sense that ours show only a small dispersion (~ 1.5 – 3 km s^{-1}) while theirs differ widely from each other (~ 0.5 – 5 km s^{-1}). Since we found that their macroturbulence velocity (which they denoted as v_{macro} in their Table A.1) does not show any $\log g$ -dependence, which is in marked contrast with our basic postulation of g -dependent macroturbulence [cf. Eq.(1) in Paper I], the difference in the treatment of macroturbulence might be the cause for this large discrepancy. For reference, our $v_e \sin i$ results are plotted against T_{eff} and M_{seis} in Figs. 9a and 9b (in analogy with Figs. 10e and 10f in Paper I), respectively. As we can see from these figures, the trends of $v_e \sin i$ in terms of these parameters are essentially the same as in Paper I (i.e., slowing-down tendency with a decrease in T_{eff} , higher $v_e \sin i$ with an increase in M).

elements (in the metallicity range of $-0.7 \lesssim [\text{Fe}/\text{H}] \lesssim +0.3$) are quite similar to Figs. 11r–11t in Paper I.

⁴ Note that the sign of the abscissa (T_{eff}) in our Figs. 7d–7f is inverse as compared with Thygesen et al.’s (2012) Fig. 2.

4 DISCUSSION

4.1 Accuracy of spectroscopic gravity

We first examine how our spectroscopically determined surface gravity is compared with the seismic gravity derived from R_{seis} and M_{seis} . Since the original R_{seis} and M_{seis} values presented by Mosser et al. (2012) correspond to Brown et al.’s (2011) photometric T_{eff} (KIC), some of which appear to show considerable errors (cf. Figs. 7a and 7d), we recalculated R_{seis} and M_{seis} by using our spectroscopic T_{eff} along with the seismic quantities [ν_{max} (central frequency of the oscillation power excess) and $\Delta\nu$ (large frequency separation)] derived by Mosser et al. (2012). For this purpose, we applied the scaling relations used by Kallinger et al. (2010a):

$$R_{\text{seis}}/R_{\odot} = (\nu_{\text{max}}/\nu_{\text{max},\odot})(\Delta\nu/\Delta\nu_{\odot})^{-2}(T_{\text{eff}}/T_{\text{eff},\odot})^{1/2} \quad (1)$$

$$M_{\text{seis}}/M_{\odot} = (\nu_{\text{max}}/\nu_{\text{max},\odot})^3(\Delta\nu/\Delta\nu_{\odot})^{-4}(T_{\text{eff}}/T_{\text{eff},\odot})^{3/2} \quad (2)$$

and

$$\begin{aligned} g_{\text{seis}}/g_{\odot} &= (M_{\text{seis}}/M_{\odot})(R_{\text{seis}}/R_{\odot})^{-2} \\ &= (\nu_{\text{max}}/\nu_{\text{max},\odot})(T_{\text{eff}}/T_{\text{eff},\odot})^{1/2}, \end{aligned} \quad (3)$$

where $\nu_{\text{max},\odot} = 3050 \text{ } \mu\text{Hz}$, $\Delta\nu_{\odot} = 134.92 \text{ } \mu\text{Hz}$, $T_{\text{eff},\odot} = 5777 \text{ K}$, and $g_{\odot} = 10^{4.44} \text{ cm s}^{-2}$. Such recalculated R_{seis} , M_{seis} , and $\log g_{\text{seis}}$ for each star are given in Table 1, and the variations relative to Mosser et al.’s (2012) original values are shown in Fig. 10. We can see from this figure that the differences in $\log g_{\text{seis}}$ are very marginal (0.01–0.02 dex in most cases) and practically negligible, because g_{seis} is insensitive to T_{eff} (i.e., $\propto T_{\text{eff}}^{1/2}$).

The comparison between $\log g_{\text{spec}}$ and $\log g_{\text{seis}}$ is displayed in Fig. 11a, and the difference $\Delta \log g$ ($\equiv \log g_{\text{spec}} - \log g_{\text{seis}}$) is plotted against T_{eff} in Fig. 11b. We can see from these figures that both are in satisfactory agreement with each other ($r = 0.96$; cf. Table 3). Actually, the mean difference averaged over all 58 stars is $\langle \Delta \log g \rangle = -0.02 \text{ dex}$ with the standard deviation of $\sigma = 0.10 \text{ dex}$.⁵ Therefore, we may conclude that our spectroscopic $\log g$ determination is sufficiently reliable, in the sense that it can be used for evaluating absolute $\log g$ values of red giants to a precision of $\simeq 0.1 \text{ dex}$.

It should be remarked, however, that this conclusion applies to the spectroscopic $\log g$ obtained by using the TGVIT program as done in Paper I. Given that the $\log g$ values spectroscopically derived in Paper I were systematically smaller than those of several other previous studies as already mentioned in Sect. 1, we may state based on the present conclusion that those “high-scale” $\log g$ results published by previous investigators are likely to be inadequately overestimated despite that they were derived in a similar spectroscopic method using Fe I and Fe II lines. Besides, although Thygesen et al. (2012) arrived at a similar result that the spectroscopic and seismic $\log g$ values are almost consistent with each other in the average sense, the mean difference was $\langle \Delta \log g \rangle = -0.05$ ($\sigma = 0.30$) for 57 stars, which means that the dispersion of deviation in their results is 3 times

⁵ If the results from two different data sets are to be separately treated, we obtain $\langle \Delta \log g \rangle = -0.03$ ($\sigma = 0.09$) for 42 stars based on our Subaru data, and $\langle \Delta \log g \rangle = +0.01$ ($\sigma = 0.12$) for 16 stars based on Thygesen et al.’s (2012) spectra.

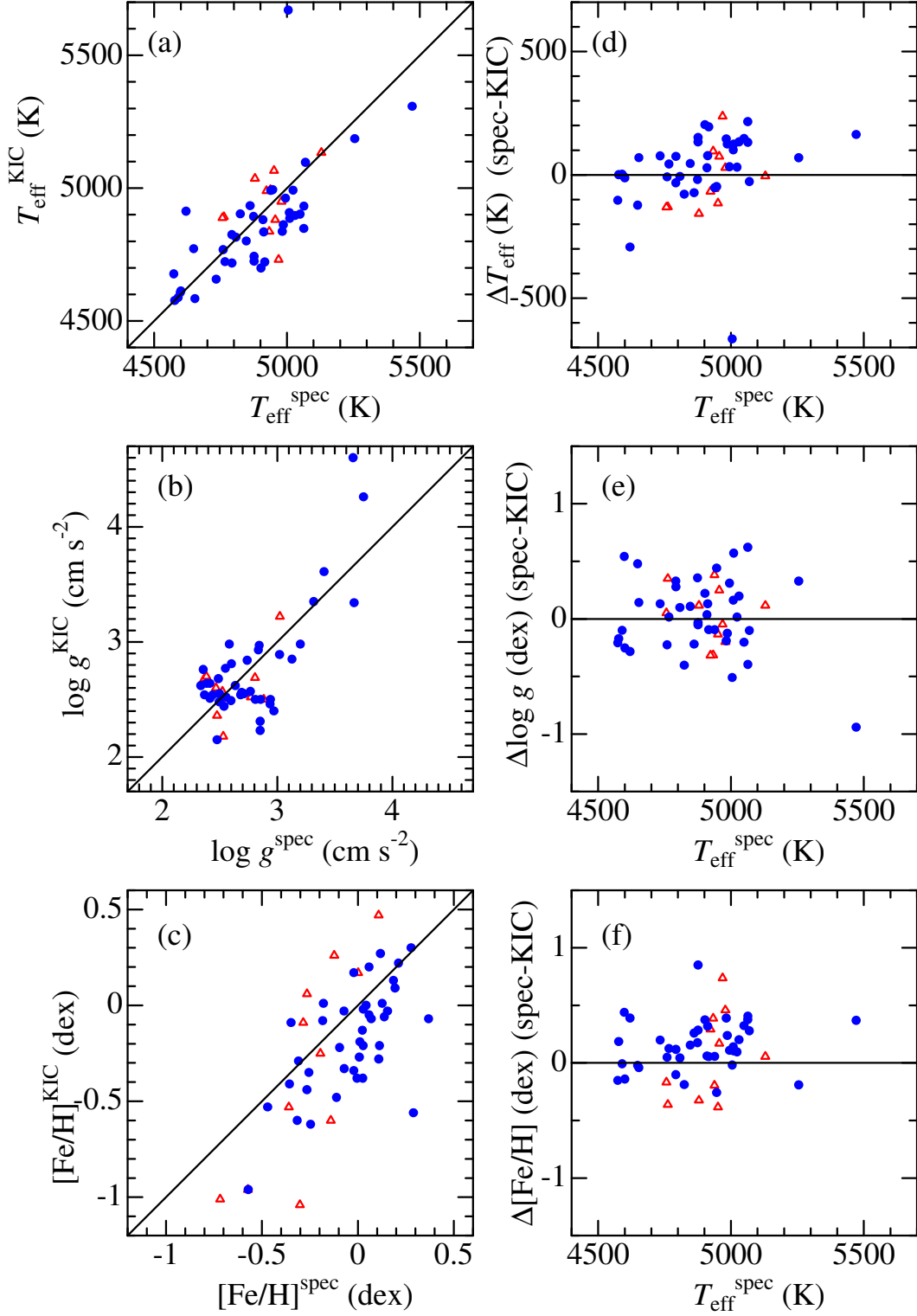


Figure 7. Comparison of T_{eff} , $\log g$, and $[\text{Fe}/\text{H}]$ given in the *Kepler* Input Catalog (Brown et al. 2011) with those we determined spectroscopically in this study. Left panels (a, b, c) are the direct comparisons between these two, while right panels (d, e, f) show the (ours–KIC) difference plotted against our spectroscopic T_{eff} . Filled circles are the results (for 42 stars) based on our Subaru/HDS spectra, while open triangles are those (for 16 stars) derived by using the NOT/CFHT/TBL spectra published by Thygesen et al. (2012).

Table 2. Parameters derived from evolutionary tracks for 9 stars with available parallaxes.

KIC# (1)	HIP# (2)	V (3)	π (4)	σ_π (5)	A_V (6)	M_V (7)	B.C. (8)	$\log L$ (9)	T_{eff} (10)	[Fe/H] (11)	M_{trk} (12)	R_{ph} (13)	M_{seis} (14)	R_{seis} (15)	class (16)	Remark (17)
03730953	93687	9.07	2.06	0.95	0.27	0.37	-0.31	1.88	4861	-0.07	2.47	12.3	1.97	11.4	RC2	
04044238	94221	8.15	4.36	0.78	0.10	1.25	-0.48	1.59	4519	+0.20	1.43	10.2	1.06	10.5	RC1	
05737655	98269	7.32	5.22	0.61	0.08	0.83	-0.26	1.67	5026	-0.63	2.08	9.1	0.78	9.2	RC1	
08813946	95005	7.19	5.04	0.59	0.09	0.61	-0.31	1.78	4862	+0.09	2.51	11.0	2.09	9.8	RC1	
09705687	94976	9.79	0.82	1.08	0.24	-0.88	-0.22	2.34	5129	-0.20	3.50	19.1	1.92	9.3	RC2	unreliable π
10323222	92885	7.01	7.73	0.61	0.08	1.37	-0.48	1.54	4525	+0.04	1.30	9.5	1.55	10.6	RG	
10404994	95687	7.67	3.76	0.65	0.11	0.44	-0.33	1.86	4803	-0.06	2.42	12.3	1.50	11.2	RC1	
10716853	93376	7.04	4.48	0.52	0.11	0.19	-0.31	1.95	4874	-0.08	2.63	13.2	1.75	10.9	RC1	
12884274	94896	7.88	3.04	0.69	0.09	0.20	-0.39	1.97	4683	+0.11	2.53	14.8	1.39	10.6	RC1	

Column (1) — KIC number, Column (2) — Hipparcos number, Column (3) — apparent visual magnitude (in mag), Column (4) — parallax (in milliarcsec), Column (5) — error of π (in milliarcsec), Column (6) — interstellar extinction (in mag), Column (7) — absolute visual magnitude (in mag), Column (8) — bolometric correction (in mag), Column (9) — $\log(\text{bolometric luminosity})$ (in L_\odot), Column (10) — spectroscopically determined T_{eff} , Column (11) — spectroscopically determined [Fe/H], Column (12) — stellar mass (in M_\odot) estimated from theoretical evolutionary tracks, Column (13) — photometric radius (in R_\odot) derived from L and T_{eff} , Column (14) — seismic mass (in M_\odot), Column (15) — seismic radius (in R_\odot), and Column (16) — evolutionary status (see the caption of Table 1). The data in Columns (2)–(5) were taken from the Hipparcos catalogue (ESA 1997). See Sect. 3.2 in Paper I for more details regarding the derivation of A_V , B.C., and M_{trk} . Note that T_{eff} , [Fe/H], M_{seis} , and R_{seis} are the same as in Table 1.

Table 3. Statistical quantities for the stellar-parameter correlations shown in figures 7, 8, 11, and 12.

Figure	X	Y	N	r	$\langle Y - X \rangle$	σ	Unit	Remark
Fig. 7a	$T_{\text{eff}}^{\text{spec}}$	$T_{\text{eff}}^{\text{KIC}}$	51	0.694	-15	146	K	
Fig. 7b	$\log g^{\text{spec}}$	$\log g^{\text{KIC}}$	51	0.739	-0.02	0.30	dex	
Fig. 7c	$[\text{Fe}/\text{H}]^{\text{spec}}$	$[\text{Fe}/\text{H}]^{\text{KIC}}$	51	0.668	-0.13	0.26	dex	
Fig. 8a	$T_{\text{eff}}^{\text{ours}}$	$T_{\text{eff}}^{\text{Thygesen}}$	16	0.868	+40	70	K	
Fig. 8b	$\log g^{\text{ours}}$	$\log g^{\text{Thygesen}}$	16	0.651	+0.01	0.20	dex	
Fig. 8c	v_t^{ours}	v_t^{Thygesen}	16	0.905	+0.13	0.04	km s ⁻¹	
Fig. 8d	$[\text{Fe}/\text{H}]^{\text{ours}}$	$[\text{Fe}/\text{H}]^{\text{Thygesen}}$	16	0.965	-0.02	0.08	dex	
Fig. 8e	$v_e \sin i^{\text{ours}}$	$v_e \sin i^{\text{Thygesen}}$	16	0.250	+0.89	1.23	km s ⁻¹	
Fig. 11a	$\log g_{\text{seis}}$	$\log g_{\text{spec}}$	58	0.960	-0.02	0.10	dex	
Fig. 12a	$\log M_{\text{seis}}$	$\log M_{\text{trk}}$	8	0.389	+0.16	0.15	dex	KIC 9705687 excluded
Fig. 12b	$\log R_{\text{seis}}$	$\log R_{\text{ph}}$	8	0.615	+0.04	0.06	dex	KIC 9705687 excluded

X and Y denote the quantities in the abscissa and ordinate of the relevant figure, respectively. while N is the number of samples used for calculating the statistical quantities: r is the correlation coefficient between X and Y , $\langle Y - X \rangle$ is the average of the difference ($Y - X$), and σ is the standard deviation. Note that logarithmic representation is used here for M and R in the last two rows, despite that these quantities are normally (i.e., linearly) represented in Fig. 12a and Fig. 12b.

as large as ours (cf. Fig. 3 in their paper).⁶ Thus, since the effectiveness of spectroscopic parameter determinations appears to be rather case-dependent, one should keep more attention to practical details involved with his method (e.g., which quality/strength and how many lines are to be used, atomic parameters, criteria level of required conditions).

4.2 Mass problem in red clump giants

In Figs. 12a and 12b are compared M_{trk} (mass estimated from evolutionary tracks) and R_{ph} (radius evaluated from L and T_{eff}) derived for 9 stars with known parallax data (cf. Table 2) to the corresponding seismic M_{seis} and R_{seis} , respectively. We see from Fig. 12b that R_{ph} and R_{seis} are almost in agreement except for KIC 09705687, for which

the result is unreliable because its parallax contains a large error. In contrast, Fig. 12a reveals that M_{trk} is considerably larger than M_{seis} roughly by $\sim 50\%$ on the average (i.e., $\sim 1\text{--}2 M_{\text{seis}}$ corresponds to $\sim 1.5\text{--}3 M_{\text{trk}}$). However, since $M_{\text{trk}} \simeq M_{\text{seis}}$ holds for KIC 10323222 (normal red giant; RG), appreciable discrepancies are likely to be seen only in red clump giants (RC1/RC2). These facts suggest that our suspicion mentioned in Sect. 1 resulting from the comparison of Figs. 2b and 2e was surely correct. That is, we must now admit that the M_{trk} values for red clump giants (roughly corresponding to the intersection of the trifid structure in Fig. 2e) derived in Paper I were erroneously overestimated.

Presumably, the cause for this disagreement is related to the process of mass determination adopted in Paper I, where Lejeune & Schaerer's (2001) grids of stellar evolutionary tracks (computed for 11 M values of 0.8, 0.9, 1.0, 1.25, 1.5, 1.7, 2.0, 2.5, 3.0, 4.0, and 5.0 M_\odot for each of the six metallicities $z = 0.001, 0.004, 0.008, 0.02, 0.04$, and 0.10) were used. That is, for a set of evolutionary tracks corresponding to each mass M_i , the minimum luminosity difference ($\delta_i \equiv \log L_i - \log L^*$, where $\log L^*$ is the given lumi-

⁶ In contrast to Thygesen et al.'s (2012) implication, we consider that LTE is practically valid in the Fe I/Fe II ionization equilibrium as far as red giant stars under study are concerned, since the deviation $\Delta \log g$ does not show any T_{eff} -dependence (cf. Fig. 11b).

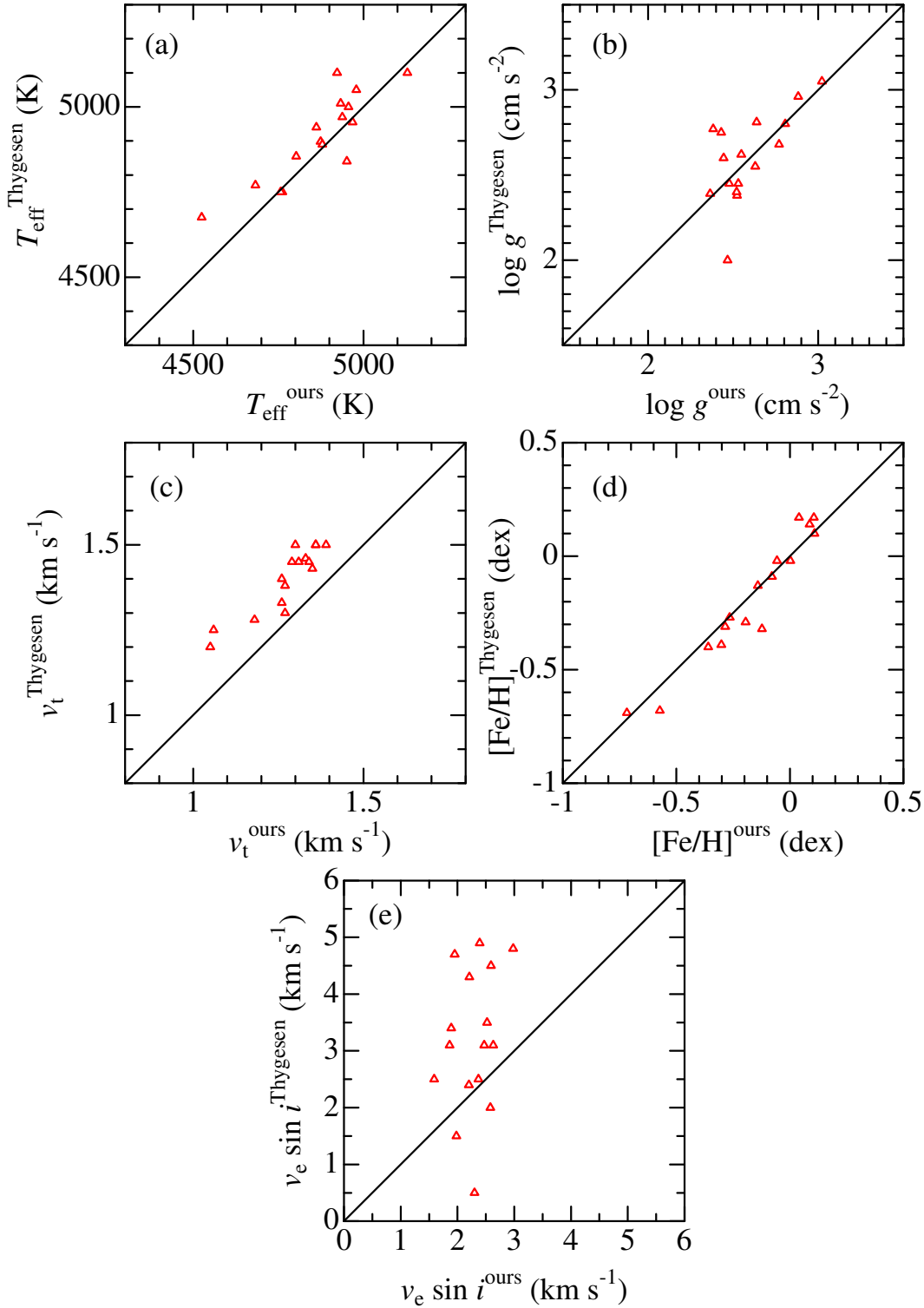


Figure 8. Comparison of our (a) T_{eff} , (b) $\log g$, (c) v_t , (d) $[\text{Fe}/\text{H}]$, and (e) $v_e \sin i$ for 16 stars spectroscopically established by using Thygesen et al's (2012) spectra with their values similarly determined based on the same data. The meaning of the symbol is the same as in Fig. 7.

osity of a star) was computed⁷ at the interpolated point(s) on the relevant track for $T_{\text{eff}} = T_{\text{eff}}^*$. Then, the best M value

(for the metallicity of the relevant tracks) accomplishing the

⁷ If several different δ values exist at a fixed T_{eff} (i.e., for the

case of a looped track), we adopt the one corresponding to the smallest $|\delta|$ among those.

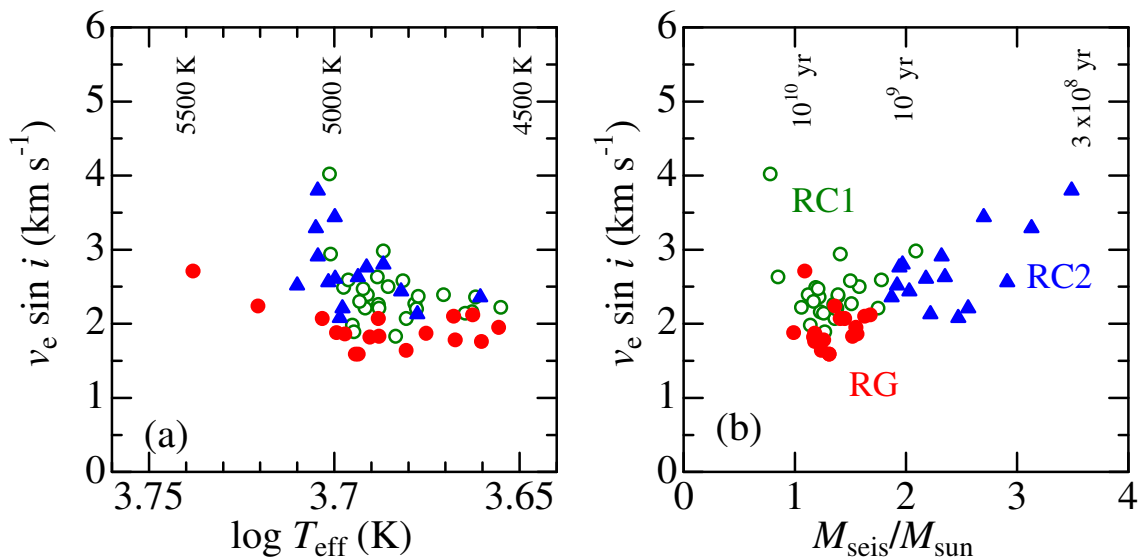


Figure 9. The $v_e \sin i$ values derived from the 6080–6089 Å fitting plotted against T_{eff} (left panel) and M_{seis} (right panel) based on the data given in Table 1. See the caption of Fig. 2 for the meanings of the symbols.

minimum $|\delta|$ was estimated by interpolation based on the set of $\{\delta_i, i = 1, 11\}$. This whole process was repeated for each set of tracks corresponding to different metallicities, and the final M value corresponding to the observed stellar $[\text{Fe}/\text{H}]$ was determined again by interpolation.

In this way of M determination for a star at the red clump luminosity of $\log(L/L_\odot) \sim 1.5$ – 2 , the result tends to be the one corresponding to the normal red giant evolution (even if it is really a red clump star), because a solution of M (for any $[\text{Fe}/\text{H}]$) accomplishing the given stellar luminosity is always found for such red giant tracks running nearly horizontally and discriminated by $(M, [\text{Fe}/\text{H}])$ (cf. Fig. 2d). Thus, $M \sim 2$ – $3 M_\odot$ would naturally obtained for those stars in the red clump zone (cf. Fig. 2e). However, actual masses of those red-clump stars in the He-burning stage to be found at $\log(L/L_\odot) \sim 1.5$ – 2 , which have returned from the RGB tip, are much smaller to be ~ 1 – $2 M_\odot$ (see, e.g., Fig. 10 in Kallinger et al. 2010b). This must be the reason for the discrepancy between M_{trk} (~ 1.5 – $3 M_\odot$) and M_{seis} (~ 1 – $2 M_\odot$) we found for red clump giants in Fig. 12a.

Interestingly, the consequence that the M values derived in Paper I are likely to be significantly overestimated for red clump giants (constituting a large fraction of 322 targets) provides a reasonable solution for the inexplicable features noted in that paper.

– First, the surface gravity ($\log g_{\text{TLM}}$) directly derived from T_{eff} , L , and M was found to be systematically larger by ~ 0.1 – 0.2 dex than the spectroscopic gravity ($\log g_{\text{spec}}$) just around $\log g \sim 2$ – 3 corresponding the red clump region (cf. Fig. 1g therein). This discrepancy can be naturally explained by an overestimation of M by $\sim 50\%$.

– Second, it was remarked in Paper I that the age vs. $[\text{Fe}/\text{H}]$ relation derived for 322 giants and that for 160 FGK dwarfs obtained by Takeda (2007) do not connect smoothly but show an appreciable discontinuity especially around $\text{age} \sim 10^9$ yr (cf. Fig. 13, which is equivalent to Fig. 14 in Paper I) That is, while the large scatter of $[\text{Fe}/\text{H}]_{\text{dwarfs}}$ seen in old stars ($\text{age} \sim 10^{10}$ yr) tends to converge toward

medium-aged stars ($\text{age} \sim 10^9$ yr), a large spread reappears in $[\text{Fe}/\text{H}]_{\text{giants}}$ at $\text{age} \sim 10^9$ yr which again shrinks toward young stars ($\text{age} \sim 10^8$ yr). However, we now know that many red clump giants should have masses around $\sim 1.5 M_\odot$ (corresponding to $\log \text{age} \sim 9.3$; cf. Fig. 3c in Paper I) instead of the previous values around $\sim 2.5 M_\odot$ ($\log \text{age} \sim 8.8$). It is gratifying to see that the increase in the age of clump giants by $\Delta \log \text{age} \sim 0.5$ dex corresponding to this revision satisfactorily removes the discrepancy between two age vs. $[\text{Fe}/\text{H}]$ distributions (cf. the arrow in Fig. 13).

4.3 Classification of red giants

Finally, let us discuss the question inspired by the similarity of Figs. 2b and 2e: “Is it possible to distinguish the different evolutionary status of red giants (RG/RC1/RC2) only by way of the conventional approach as adopted in Paper I?” We now know that the spectroscopic $\log g$ values are sufficiently reliable, while the M values estimated from theoretical tracks as done in Paper I are erroneously too large typically by $\sim 50\%$ for clump giants (RC1/RC2) though they are still reasonably usable for normal H-burning red giants (RG). Keeping this information in mind, we can roughly figure out the classification of many red giants plotted in Fig. 2e (gray symbols). For example, a bunch of stars located in the region of lower M but higher $\log g$ ($1 \lesssim M_{\text{trk}}/M_\odot \lesssim 2$ and $2.5 \lesssim \log g_{\text{spec}} \lesssim 3.5$) presumably belong the RG class. Most of the stars densely populated in the heart of Fig. 2e ($2 \lesssim M_{\text{trk}}/M_\odot \lesssim 3$ and $2 \lesssim \log g_{\text{spec}} \lesssim 3$) are likely to be in the red clump (RC1/RC2) category, despite that their M_{trk} values are systematically overestimated compared to the true values. But unfortunately, reliable classification for each star in this crowded clump region is very difficult, especially regarding the distinction of RC1 and RC2 where information of absolute M values is required, as $M_{\text{seis}} = 1.8 M_\odot$ was adopted by Mosser et al. (2012) for the distinction limit between these two. Since this critical mass value al-

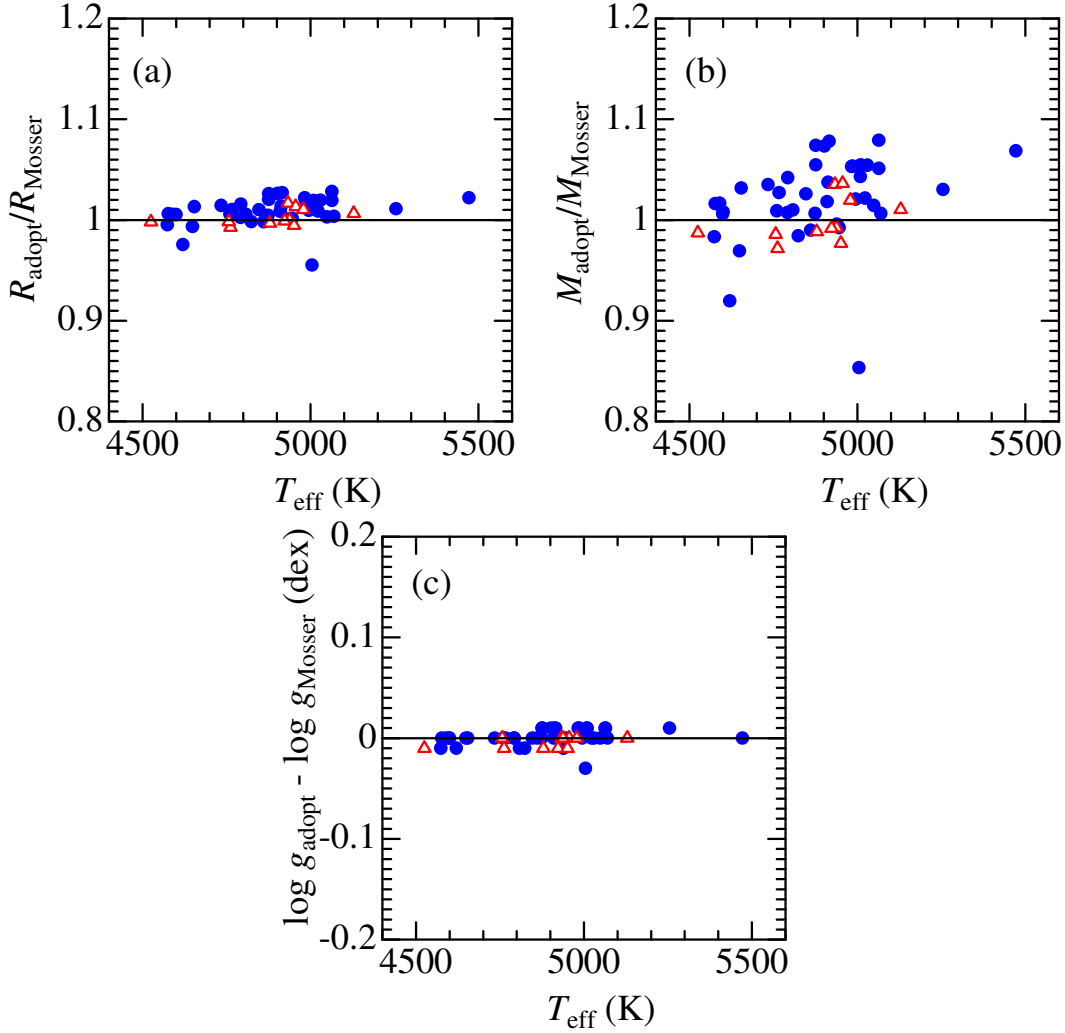


Figure 10. Variations between the finally adopted seismic R , M , and $\log g$ [obtained by applying our spectroscopic T_{eff} to Eqs. (1)–(3)] and Mosser et al.’s (2012) original values [based on $T_{\text{eff}}(\text{KIC})$], plotted against T_{eff} . The meanings of the symbols are the same as in Fig. 7.

most coincides with the intersection point of “trifid” structure in Fig. 2b, the corresponding value in Fig. 2e might be $M_{\text{trk}} \sim 2.5 M_{\odot}$ where the intersection in the similar distribution is seen. However, the real situation should not be so simple as such a naive analogy, since the required correction in M_{trk} must be different between RG and RC1/RC2, which makes us rather cautious in placing too much weight on the similarity of Figs. 2b and 2e. Thus, we have to conclude that the approach of Paper I (at least in the present level) can not be so effective as the asteroseismic technique in distinguishing the evolutionary status of red giants from the viewpoint of accuracy.⁸

⁸ In connection with this conclusion, we first expected that $v_e \sin i$ may be used to discriminate between RG and RC1/RC2, since their different evolution histories might have resulted in different degree of angular momentum loss. While we notice in Figs. 9a and 9b that $v_e \sin i(\text{RG})$ tend to be smaller than $v_e \sin i(\text{RC1/RC2})$, we feel it still premature to take this trend as very meaningful, since RG-class stars in our sample are biased to smaller masses ($M_{\text{seis}} \sim 1\text{--}2 M_{\odot}$). That is, this apparent trend

Nevertheless, we consider that this conventional procedure (spectroscopic method coupled with the help of stellar evolutionary tracks) may possibly be improved to a practicable level, though this assumes that reliably accurate parallax data are available as a prerequisite. For example, we would be able to derive two kinds of M_{trk} for a star locating in the clump region on the HR diagram while *assuming* its status (i.e., either H-burning RG or He-burning RC) in advance, where much more refined evolutionary tracks with finer mass steps (e.g., $0.1 M_{\odot}$) should be used such as shown in Fig. 10 of Kallinger et al. (2010b). Which of these two solutions of $M_{\text{trk}}(\text{RG})$ and $M_{\text{trk}}(\text{RC})$ represents the truth may be judged from the $\log g_{\text{spec}}$ vs. R_{ph} relation where RG and RC tend to dwell rather separately (cf. Fig. 2f in comparison with Fig. 2c), because we may hope that these two quantities can

may be simply due to the M -dependence of $v_e \sin i$. In order to check whether or not this tendency really reflects the evolution-related effect, the sample would have to be further increased so that stars of all three classes may be available over a sufficiently wide range of M .

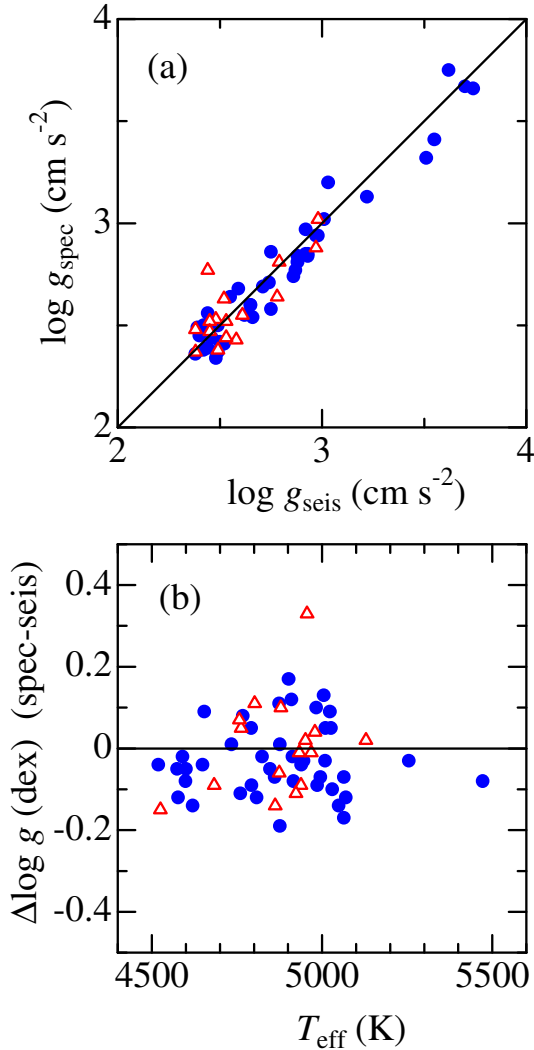


Figure 11. (a) Comparison of our spectroscopic $\log g_{\text{spec}}$ with the seismic $\log g_{\text{seis}}$. (b) Plot of the $\log g$ difference [$\Delta \log g (\equiv \log g_{\text{spec}} - \log g_{\text{seis}})$] against T_{eff} . The meanings of the symbols are the same as in Fig. 7.

be well established (given that accurately known distance allows a reliable evaluation of L). Or alternatively, this decision could be made by checking the consistency between $\log g_{\text{TLM}}$ and $\log g_{\text{spec}}$ (cf. Sect. 4.2). Then, if $M_{\text{trk}}(\text{RC})$ turned out to be the correct solution, the distinction between RC1 and RC2 is straightforward from its comparison with the critical mass ($\sim 1.8 M_{\odot}$).

In any event, availability of reliable parallax data is essential for such a method of approach to work successfully, since precisely evaluated L (along with spectroscopically determined T_{eff} and $[\text{Fe}/\text{H}]$) is necessary for correctly setting the position of a star on the $\log L$ vs. $\log T_{\text{eff}}$ diagram, which should be compared with theoretical tracks to determine M . It is unfortunate that parallaxes are currently known (even so, the accuracy is not yet sufficient) for only a limited number of Mosser et al.'s (2012) *Kepler* giants with asteroseismologically established classification and seismic parameters (e.g., only 9 out of 55 targets in the present case). We expect, however, that this situation will soon be significantly improved by the high-precision parallax data to

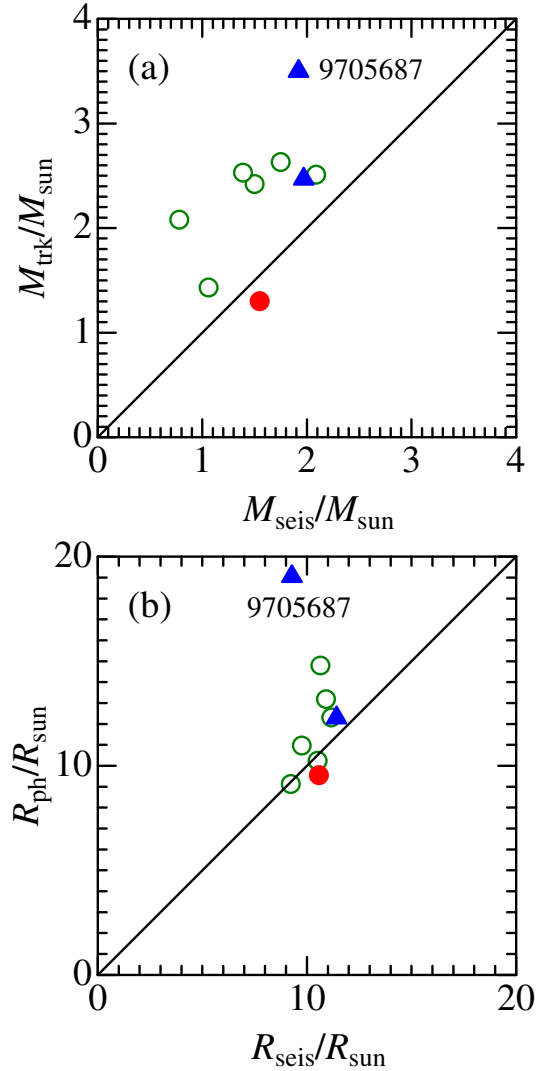


Figure 12. Comparison of seismic mass or radius with those evaluated in the conventional approach for 9 stars, for which parallax data are available (see Table 2). Upper panel (a): M_{trk} (mass estimated from evolutionary tracks) vs. M_{seis} (seismic mass). Lower panel (b): R_{ph} (photometric radius derived from L and T_{eff}) vs. R_{seis} (seismic radius). See the caption of Fig. 2 for the meanings of the symbols.

be released by Gaia. After very precise distance data have been established for all these red giants with known seismic properties, we would like to revisit this problem by carrying out a renewed analysis similar to this study (hopefully based on more extended samples), in order to see whether such an approach of diagnosing the nature of red giants we propose efficiently works out.

5 SUMMARY AND CONCLUSION

Recent progress in asteroseismology based on very high-precision photometry from satellites such as *Kepler* has enabled to successfully sort out the various complex evolutionary stages of many red giants [either normal H-burning giants (RG) ascending the RGB or He-burning giants (RC1/RC2) residing in the 1st or 2nd clump after re-

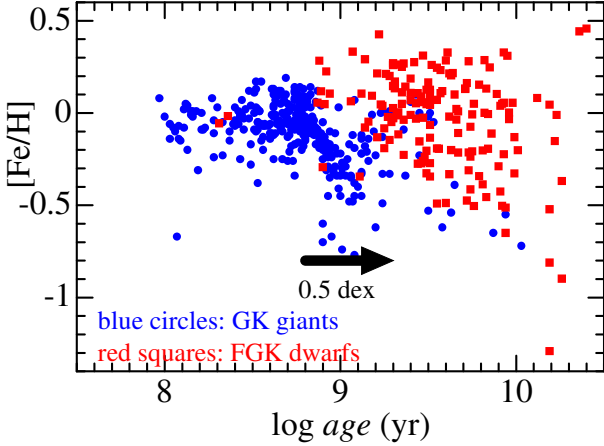


Figure 13. Metallicity ($[\text{Fe}/\text{H}]$) vs. *age* relation for 322 G-K giants (circles) based on the results of Paper I and for 160 FGK dwarfs based on the results of Takeda (2007). The arrow indicates the increase of age to be applied to red clump giants (from $\log \text{age} \sim 8.8$ to $\log \text{age} \sim 9.3$ by ~ 0.5 dex) resulting from the downward revision of their masses (cf. the last paragraph in Sect. 4.2) Note that this figure is essentially the same as Fig. 14 in Paper I.

turning from the RGB tip)] as well as to precisely determine their mass and radius.

When the correlations of such seismic parameters (M_{seis} , R_{seis} , and $\log g_{\text{seis}}$) established by Mosser et al. (2012) for ~ 200 red giants observed by *Kepler* were compared with those previously determined in Paper I for a large number of field G–K giants based on the conventional approach (i.e., spectroscopic T_{eff} , $\log g$, v_t , and $[\text{Fe}/\text{H}]$ based on the equivalent widths of Fe I and Fe II lines, while M and R evaluated from L with the help of stellar evolutionary tracks), we noticed an interesting similarity in the $\log g$ vs. M diagram, where the seismic parameters of different evolutionary classes show characteristic distributions, which implied that even such an ordinary approach as adopted in Paper I might possibly be used for distinguishing the complex evolutionary stages of red giants.

As a first step toward this possibility, we decided to examine the precision of conventionally derived $\log g$ and M in reference to the seismic values. For this purpose, we applied the same parameter determination method as adopted in Paper I to selected 55 red giants in the *Kepler* field, for which seismic parameters and evolutionary classes are well defined by Mosser et al. (2012).

The spectroscopic parameters were derived by using the TGVIT program (Takeda et al. 2005) with the equivalent widths of Fe I and Fe II lines measured mainly on the high-dispersion spectra obtained by Subaru/HDS (42 stars) while partly on the spectra published by Thygesen et al. (2012) (16 stars). We also derived $v_e \sin i$ (projected rotational velocity) from the line-broadening width by a spectrum-fitting analysis in the 6080–6089 Å region as in Paper I.

It was confirmed that our spectroscopic gravity ($\log g_{\text{spec}}$) and the seismic gravity ($\log g_{\text{seis}}$) are in satisfactory agreement with each other (to within $\simeq 0.1$ dex) without any systematic difference, which ensures the reliability of our spectroscopic parameters based on Fe I and Fe II lines.

For 9 stars for which parallax data are available among these spectroscopic targets, the stellar parameters relevant to the HR diagram (L , M_{trk} , and R_{ph}) were also determined. While we found a reasonable consistency between R_{ph} and R_{seis} (except for 1 star with an unreliable parallax), the masses of He-burning red clump giants derived from evolutionary tracks turned out to be $M_{\text{trk}}(\text{RC1}/\text{RC2}) \sim 2\text{--}3 M_{\odot}$, which are markedly larger by $\sim 50\%$ than the seismic results of $M_{\text{seis}}(\text{RC1}/\text{RC2}) \sim 1\text{--}2 M_{\odot}$, though such discrepancy is not apparent for normal H-burning giants [$M_{\text{trk}}(\text{RG}) \simeq M_{\text{seis}}(\text{RG})$]. This disagreement is presumably attributed to the difficulty of mass determination from the evolutionary tracks where RG paths (higher M) and RC paths (lower M) are intricately overlapping at the same clump region of the HR diagram; i.e., simply running RG tracks tend to be preferentially used even for RC stars.

This consequence naturally implies that many of the M_{trk} values of 322 red giants (most of them are likely to be red clump stars) estimated in Paper I were erroneously overestimated by an order of $\sim 50\%$, about which serious caution should be taken, though other results (e.g., R_{ph} values or spectroscopic parameters) derived therein do not have any problem. The fact that an upward revision by $\sim 50\%$ for the mass values in Paper I removes the puzzling discrepancy found in Paper I (i.e., systematic difference between $\log g_{\text{spec}}$ and $\log g_{\text{TLM}}$, a mismatch between dwarfs and giants in the distribution of $[\text{Fe}/\text{H}]$ vs. *age* diagram) substantiates this conclusion.

We must conclude that the traditional approach of Paper I is not so effective as the asteroseismic technique in distinguishing the evolutionary status of red giants. However, it may be still useful (at least for guessing the evolutionary class) if parallaxes are reliably determined (for accurate estimation of L) and up-to-date theoretical tracks (covering the whole RG–RC stage with a sufficiently small M step) are used, since we may hope that T_{eff} , $\log g$, and $[\text{Fe}/\text{H}]$ can be reliably determined spectroscopically. Above all, the availability of precise distances is essential. When very accurate parallax data have become available in the near future for the reference giants with known seismic properties, it would be worth carrying out a renewed analysis similar to this study, in order to check whether such a conventional approach for diagnosing the nature of red giants really works out.

ACKNOWLEDGMENTS

This research has been carried out by using the SIMBAD database, operated by CDS, Strasbourg, France.

REFERENCES

- Bressan A., Marigo P., Girardi L., Salasnich B., Dal Cero C., Rubele S., Nanni A., 2012, MNRAS, 427, 127
- Bressan A., Marigo P., Girardi L., Nanni A., Rubele S., 2013, EPJ Web of Conferences, 43, 3001 (DOI: <http://dx.doi.org/10.1051/epjconf/20134303001>)
- Brown T. M., Latham D. W., Everett M. E., Esquerdo G. A., 2011, AJ, 142, 112
- ESA 1997, The Hipparcos and Tycho Catalogues, ESA SP-1200 (Noordwijk: ESA)

- Girardi L., 1999, MNRAS, 308, 818
 Kallinger T. et al., 2010a, A&A, 509, A77
 Kallinger T. et al., 2010b, A&A, 522, A1
 Lagarde N., Decressin T., Charbonnel C., Eggenberger P., Ekström S., Palacios A., 2012, A&A, 543, A108
 Lejeune T., Schaerer D., 2001, A&A, 366, 538
 Mosser B. et al., 2012, A&A, 540, A143
 Noguchi K. et al., 2002, PASJ, 54, 855
 Pietrinferni A., Cassisi S., Salaris M., Castelli F., 2004, ApJ, 612, 168
 Tajitsu A., Aoki W., Yamamuro T., 2012, PASJ, 64, 77
 Takeda Y., 2007, PASJ, 59, 335
 Takeda Y., Ohkubo M., Sadakane K., 2002, PASJ, 54, 451
 Takeda Y., Ohkubo M., Sato B., Kambe E., Sadakane K., 2005, PASJ, 57, 27 (Erratum 57, 415)
 Takeda Y., Sato B., Murata D., 2008, PASJ, 60, 781 (Paper I)
 Thygesen A. O. et al., 2012, A&A, 543, A160

APPENDIX A: RECENT HIGH-RESOLUTION GRID OF STELLAR EVOLUTIONARY TRACKS

We discussed in Sect. 4.3 the prospect of reliably determining the mass of red giants, where we suggested to derive two kinds of stellar masses by assuming its evolutionary status in advance (i.e., either RG or RC) and then adopt the more reasonable alternative. But this assumes the application of evolutionary tracks with sufficiently fine parameter grid as prerequisite, since those used in Paper I ($\Delta M/M \sim 20\text{--}30\%$, $\Delta \log z \sim 0.3\text{--}0.4$ dex; cf. Sect. 4.2) were evidently not satisfactory in this respect. How is the current situation regarding this point?

Fortunately, thanks to the remarkable progress in this field, such theoretical tracks of sufficiently high-resolution grid have already been published by several groups. For example, the BaSTI database⁹ (Pietrinferni et al. 2004) provides tracks with grids of $\Delta M/M \sim 5\text{--}10\%$ (for $\sim 1\text{--}4 M_\odot$ stars) and $\Delta \log z \sim 0.1\text{--}0.2$ dex (for the metallicity range of disk population), which were used by Kallinger et al. (2010b) and proved to be useful for discussing the parameters of red giants. More noteworthy is the recent contribution of the Padova–Trieste group, who published extensive data of evolutionary tracks and isochrones¹⁰ computed based on the PARSEC code (Bressan et al. 2012, 2013) with generally very fine grids of $\Delta M/M \sim 2\text{--}5\%$ ($0.05 M_\odot$ step for $1\text{--}2.3 M_\odot$ and $0.1 M_\odot$ step for $2.3\text{--}5 M_\odot$) and $\Delta \log z \sim 0.1$ dex. Even results of further finer mass step ($0.025 M_\odot$) are provided around $1.7\text{--}2 M_\odot$, which makes this database especially suitable for revealing the complex behavior of tracks in the red-clump region.

As a demonstration, these PARSEC tracks of near-solar metallicity ($z = 0.02$; Z0.02Y0.284.tar.gz) in the mass range $1\text{--}4 M_\odot$ (with $\Delta M = 0.05 M_\odot$ in $1\text{--}2.3 M_\odot$, while $\Delta M = 0.1 M_\odot$ in $2.3\text{--}4 M_\odot$) around the red-clump region are depicted in Fig. A1a/a' (before He ignition) and Fig. A1b/b' (after He ignition). For comparison, the tracks of Lejeune & Schaerer (2001), which were used for evaluating M_{trk} in Paper I as well as in Sect. 3.3, are shown in Fig. A1c

and Fig. A1d, each corresponding to the phase of H-burning and He-burning, respectively.

We can immediately recognize from these figures that considerable improvements in accuracies of mass determination are expected by using these recent PARSEC tracks, in comparison to the previous case of Paper I where coarse tracks were used. The distinct merit is that we do not have to worry any more about difficulties and uncertainties involved in interpolating (or extrapolating) the grid of tracks. Of course, since actual tracks are not simple and complexities (e.g., looped or bumped features) more or less exist especially at the post He-ignition phase (Fig. A1b/b'), some uncertainties are naturally inevitable. Yet, we presume that M would be determinable to a precision of $\lesssim 10\%$ (given that whether pre- or post-He ignition is presupposed) by using these evolutionary tracks in the near future, when L has been reliably established based on the very accurate parallax data to be released by Gaia, while T_{eff} and z are expected to be settled spectroscopically with sufficient accuracies (< 0.01 dex in $\log T_{\text{eff}}$ and < 0.1 dex in $\log z$).

⁹ Available from <http://albione.oa-teramo.inaf.it/>

¹⁰ Available from <http://stev.oapd.inaf.it/parsec.v1.0/> or <http://people.sissa.it/~sbressan/parsec.html>

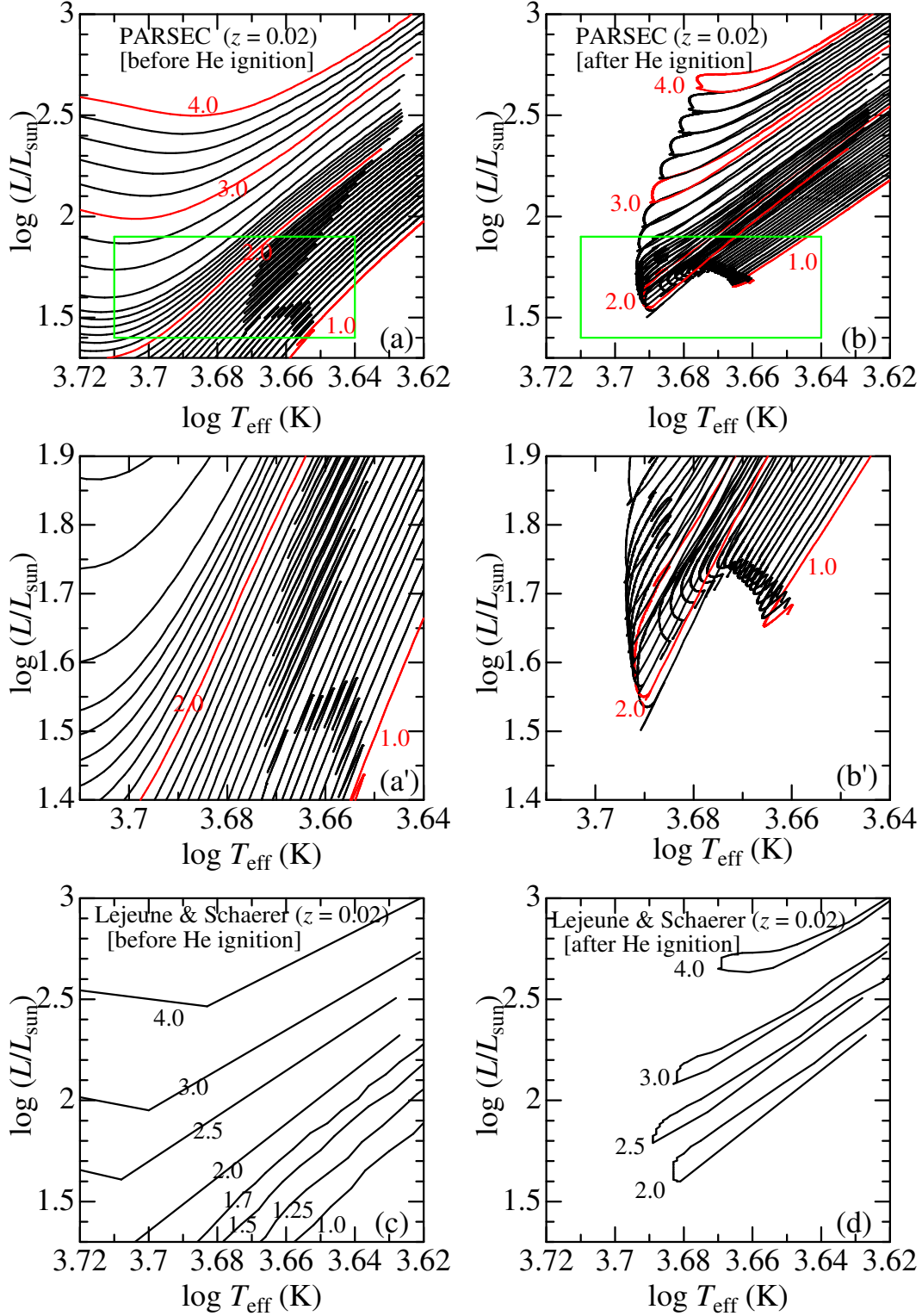


Figure A1. Top two panels: Theoretical evolutionary tracks for 1–4 M_{\odot} stars of near-solar metallicity ($z = 0.02$) around the red-clump region with high-resolution mass steps ($0.05 M_{\odot}$ for 1–2 M_{\odot} stars, $0.2 M_{\odot}$ for 2–4 M_{\odot} stars), which were calculated by the Padova–Trieste group with the PARSEC code (Bressan et al. 2012, 2013). In the left panel (a) are shown the tracks corresponding to the shell H-burning phase before He ignition, while the right panel (b) presents those of the core He-burning phase after He ignition. The tracks for 1, 2, 3, and 4 M_{\odot} are colored in red for convenience. Middle two panels: The left (a') and right (b') panels show magnification of the red-clump area indicated by green rectangles in the upper panels (a) and (b), respectively. Bottom two panels: Lejeune & Schaerer's (2001) $z = 0.02$ tracks with rather coarse mass grid (which were used for mass determination in Paper I as well as in Sect. 3.3 in this paper). The left panel (c) corresponds to the pre-He ignition phase, while the right panel (d) to the post-He ignition.